A Practical Temperature and Emissivity Separation Framework With Reanalysis Atmospheric Profiles for Hyper-Cam Airborne Thermal Infrared Hyperspectral Imagery

Lyuzhou Gao, *Member, IEEE*, Yanfei Zhong, *Senior Member, IEEE*, Liqin Cao, Jiani He, and Xuhe Zhu

***Abstract*—Compared with land surface temperature (LST) and land surface emissivity (LSE) retrieval from single-band or multispectral thermal infrared (TIR) data, TIR hyperspectral imagery allows us to obtain accurate LST and LSE through the use of an automatic temperature and emissivity separation (TES) method. However, the existing TES algorithms have rarely been investigated with airborne TIR hyperspectral imagery from the Hyper-Cam sensor, which is based on Fourier transform infrared technology. In this article, a practical LST and LSE retrieval framework incorporating reanalysis atmospheric profiles is proposed for use with Hyper-Cam airborne TIR hyperspectral imagery. In this framework, an atmospheric compensation method is introduced based on spatiotemporal analysis and the fusion of three types of widely used atmospheric profiles to replace the unattainable synchronously measured atmospheric profiles. An empirically constrained TES method is then proposed to extend the original TES algorithm to Hyper-Cam hyperspectral imagery. In addition, to exclude the negative effects of radiometric calibration error, measurement noise, and the atmospheric absorption lines in certain bands, the problematic bands are removed to improve the data quality. To evaluate the performance of the proposed framework, a set of airborne TIR hyperspectral imagery with 81 bands was acquired using the Hyper-Cam airborne system. Experiments were carried to compare the performance of the proposed method and the Fast Line-of-sight Atmospheric Analysis of Spectral Hypercubes-Infrared (FLAASH-IR) method. The results indicate that the proposed method can obtain more robust and accurate results than FLAASH-IR, and the root-mean-square error (RMSE) of the emissivity data is around 0.015 for all the validation samples.**

***Index Terms*—Airborne remote sensing, atmospheric compensation (AC), Hyper-Cam, temperature and emissivity separation (TES), thermal infrared (TIR) hyperspectral imagery.**

Manuscript received August 13, 2021; revised November 20, 2021; accepted December 6, 2021. Date of publication December 17, 2021; date of current version January 10, 2022. This work was supported in part by the National Key Research and Development Program of China under Grant 2020YFC1522703, and in part by the National Natural Science Foundation of China under Grant 42071350. *(Corresponding authors: Yanfei Zhong; Liqin Cao.)*

Lyuzhou Gao, Yanfei Zhong, Jiani He, and Xuhe Zhu are with the State Key Laboratory of Information Engineering in Surveying, Mapping, and Remote Sensing, Wuhan University, Wuhan 430079, China (e-mail: gaolyuzhou@whu.edu.cn; zhongyanfei@whu.edu.cn; hejiani@whu.edu.cn; zhuxuhe@whu.edu.cn).

Liqin Cao is with the School of Printing and Packaging, Wuhan University, Wuhan 430079, China (e-mail: clq@whu.edu.cn).

Digital Object Identifier 10.1109/JSTARS.2021.3136194

I. Introduction

THERMAL infrared (TIR) hyperspectral remote sensing, as a new observation technology, can simultaneously provide land surface temperature (LST) and land surface emissivity (LSE) information [1], [2], which is used in many applications, including precise mineral mapping [3]–[5] and target detection [6], [7]. In earlier research, LST and LSE retrieval has been mainly conducted using single-band TIR imagery or multispectral TIR imagery [8]. Typical examples are the Landsat thematic mapper sensor and the moderate resolution imaging spectrometer. Correspondingly, many LST and LSE inversion methods have been developed for use with these spaceborne data with single or multiple infrared channels, such as the single-channel algorithm [9] and the split-window algorithm [10]. However, because of the limited channel number, the inversed emissivity spectra cannot highlight the subtle features of land surface objects.

In recent years, TIR hyperspectral sensors have been developed, which can capture more abundant spectral information with hundreds of contiguous channels via airborne platforms. Examples are the spatially enhanced broadband array spectrograph system and the HyTES sensor, which have been designed primarily for experimental research, and the TASI-600 sensor and the Hyper-Cam sensor, which have been designed for remote sensing applications [11]. Differing from LST and LSE retrieval based on single-band or multispectral data, which requires many assumptions and much prior knowledge [12], TIR hyperspectral imagery does not require the use of hypothetical prerequisites and allows us to retrieve accurate LST and LSE.

Generally speaking, LST and LSE retrieval from TIR hyperspectral imagery involves two stages: 1) atmospheric compensation (AC) and 2) temperature and emissivity separation (TES) [2]. In the AC stage, the effects of atmospheric transmission losses and emissions are removed from the at-aperture radiance spectrum to obtain the ground radiance. There are two families of AC methods: 1) model-based methods [13], [14] and 2) in-scene methods [15]. The model-based AC methods have been widely used in many LST and LSE retrieval studies for their practicability and simplicity [16]–[18]. For this approach, synchronously measured atmospheric sounding profiles are needed for simulating the AC parameters. However, synchronous atmospheric

profiles are not easy to obtain. In the TES stage, the LST and LSE are concurrently determined from the ground radiance through the use of a TES algorithm. To date, a number of TES algorithms have been developed. In 1998, Borel [19] proposed the iterative spectrally smooth temperature and emissivity separation (ISSTES) algorithm and Gillespie *et al*. [20] designed the advanced spaceborne thermal emission and reflection radiometer (ASTER)–TES algorithm for use with ASTER multispectral data. In the following years, canonical correlation analysis TES [21], linear spectral emissivity constraint TES [22], and the Fast Line-of-sight Atmospheric Analysis of Spectral Hypercubes-Infrared (FLAASH-IR) method [5] were successively proposed. However, in practice, almost all of the existing TES algorithms were developed based on specific sensor data, and have rarely been investigated with Hyper-Cam airborne TIR hyperspectral imagery.

The Hyper-Cam system is a TIR hyperspectral imager based on Fourier transform infrared (FTIR) technology [23], which can achieve a relatively high spectral resolution of up to 0.25 cm^{-1}. To date, LST and LSE retrieval from Hyper-Cam airborne imagery has mainly adopted the FLAASH-IR method. FLAASH-IR is an integrated algorithm including both AC and TES stages, which has been packaged into commercial software [24]. In this method, the AC parameters are estimated from the TIR hyperspectral imagery itself, based on a smoothness criterion [25], via a look-up table, which is generated by the MODTRAN model. An extension of the ISSTES algorithm is then used for determining the final LST and LSE. However, because of the complicated imaging conditions and the short exposure time, the Hyper-Cam airborne TIR hyperspectral imagery often contains a high level of noise, which can reduce the effectiveness of the emissivity smoothness criterion. In practice, the AC and TES stages of FLAASH-IR are highly reliant on the emissivity smoothness criterion. As a result, FLAASH-IR tends to obtain unreasonable AC parameters and poor LST and LSE results for airborne TIR hyperspectral imagery that is affected by measurement noise.

In this article, to solve the problems of FLAASH-IR, a practical LST and LSE retrieval framework incorporating reanalysis atmospheric profiles is proposed for use with Hyper-Cam airborne TIR hyperspectral imagery. The main contributions of this article are summarized as follows:

1) A practical LST and LSE retrieval framework is proposed for use with Hyper-Cam airborne TIR hyperspectral imagery. To improve the data quality, the problematic bands severely affected by measurement noise, radiometric calibration error, and atmospheric absorption lines are removed through the use of quantitative data analysis and band selection.
2) Reanalysis atmospheric profiles based on the spatiotemporal analysis and fusion of different atmospheric profiles are incorporated. Three types of widely used atmospheric profiles are compared via interpolation to the same time and space. The selected optimal atmospheric profiles and ground-measured meteorological data are then fused to replace synchronously measured sounding profiles.
3) An empirically constrained TES method is proposed to extend the original TES algorithm, which was initially designed for multispectral data. The empirical constraint relationship between the maximum and minimum difference (MMD) and the minimum emissivity were rebuilt to extend the original TES algorithm to Hyper-Cam airborne hyperspectral imagery.

TABLE I
BASIC SPECIFICATIONS OF THE HYPER-CAM-LW SENSOR

Specification	Unit	Value
Spectral range	μm	7.8–11.8
Spectral resolution	cm^{-1}	0.25–150(adjustable)
FPA format	none	320 × 256
FOV	°	6.4 × 5.1
IFOV	$mrad$	0.35
Quantitative value	bit	16

The rest of this article is organized as follows. Section II introduces the Hyper-Cam sensor and the airborne campaign conducted for the TIR hyperspectral imagery collection. Section III then briefly reviews the theoretical background and the FLAASH-IR algorithm. Section IV describes the details of the proposed practical retrieval framework for Hyper-Cam airborne TIR hyperspectral imagery. In Section V, we evaluate and discuss the results of FLAASH-IR and the proposed method, according to *in-situ* measurements. Finally, Section VI concludes the article.

II. HYPER-CAM SENSOR AND AIRBORNE DATA

A. Hyper-Cam Sensor

The Hyper-Cam-LW airborne system adopted in this article is a Fourier transform TIR hyperspectral imager developed by Canada Telops Inc [5]. The spectral resolution is adjustable, and can reach up to 0.25 cm^{-1}. There are two internal blackbodies for high-quality radiometric calibration. The Hyper-Cam-LW sensor can be mounted on an aircraft through the airborne module. Table I provides a summary of the specifications of the Hyper-Cam LW sensor.

B. Experimental Data Collection

A flight campaign was conducted in 2019 in the city of Zhengzhou, Henan province, China. In addition, a field campaign was also synchronously carried out to obtain the real LST and LSE of the ground validation samples during the flight campaign.

1) Airborne Imagery Collection: The flight area was located around 30 km west of the city of Zhengzhou, which is the capital city of Henan province. The total flight area extended from 34 °47’48.94“N to 34 °51’55.56”N and 113 °16’3.27“E to 113 °17’6.26”E. Two sites were selected to collect the synchronous ground measurements: the airport site and the Dongguo Lake park site. In this article, images covering these two sites were used to facilitate the retrieval validation, as shown in Fig. 1.

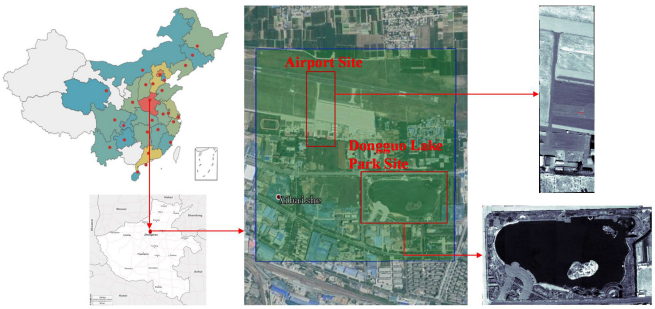

Fig. 1. Location and land cover of the two study areas.

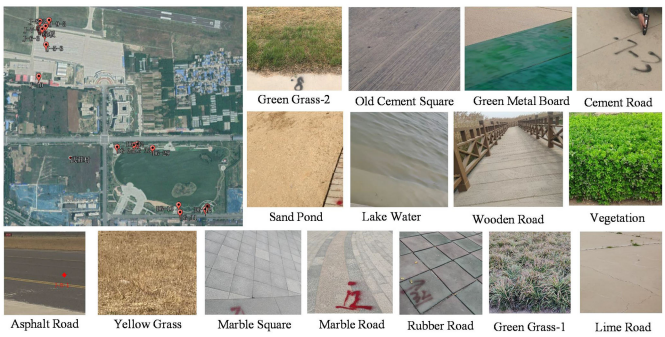

Fig. 2. Land-cover samples for the temperature measurements and their locations.

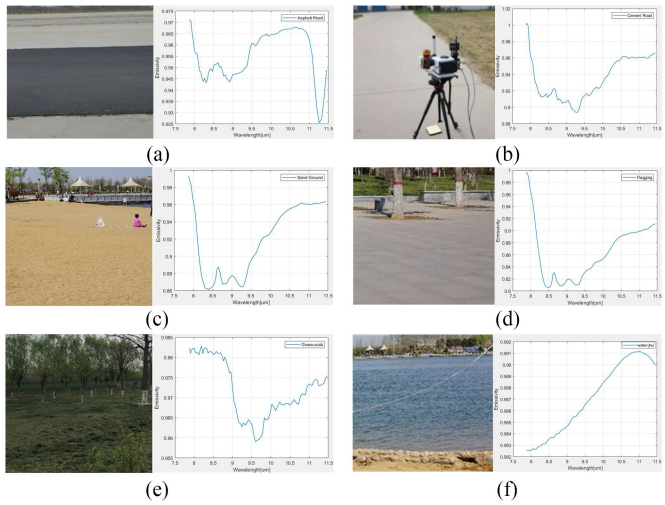

Fig. 3. Samples for the LSE measurements: (a) asphalt road, (b) cement road, (c) sandy ground, (d) flagging road, (e) green grassland, and (f) lake water.

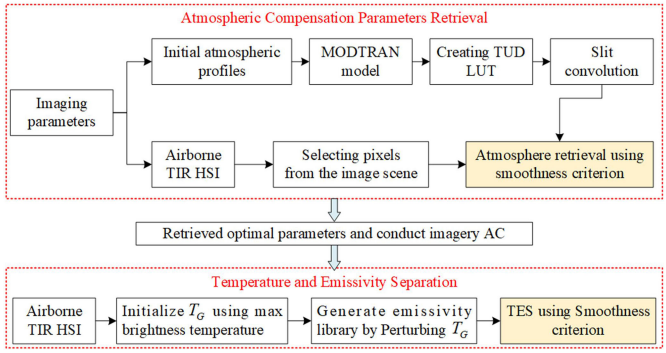

Fig. 4. Processing framework of the FLAASH-IR method.

The flight height above ground level was around 2.5 km, with a spatial resolution of around 0.95 m for a single pixel. The cool and warm blackbodies were set to 10 °C and 30 °C, respectively. The spectral resolution was set to 6 cm^{-1}. The flight campaign started at 02:00 UTC and finished at 04:10 UTC. The airport site is relatively simple, and the land surface is mainly made up of large areas of cement, grass, and asphalt. As for the Dongguo Lake park site, it includes a variety of vegetation types, artificial objects, and a large freshwater lake.

2) In-Situ *Data Measurements:* During the flight campaign, a field campaign was simultaneously performed to acquire the LST and LSE at the ground level. Two different broadband and hyperspectral thermal radiometers were used: a DX 501 thermometer and a Turbo FT spectrometer. The DX 501 is a broadband infrared thermometer for temperature measurement, and the Turbo FT is a portable hyperspectral instrument that can acquire LST and LSE simultaneously. The precision of both instruments is usually within 0.2 K for temperature measurements.

Six kinds of homogeneous land surfaces were measured for recording emissivity spectra: sandy ground, cement road, asphalt road, flagging road, green grassland, and lake water (as shown in Fig. 12). The emissivity spectra of the first four land-cover samples were measured using the Turbo FT sensor, with a spectral resolution of 4 cm^{-1}. Because of the radiance features of green grassland and cold water, the emissivity spectra extracted from the Johns Hopkins University (JHU) spectral library were deemed the true spectra [26]. The temperature of each sample was measured using the DX501 broadband thermal radiometer, and the average value of about five measurements for each sample was regarded as the true temperature for the sample. The land-cover samples for the temperature and emissivity measurements are presented in Figs. 2 and 3, respectively.

III. Theoretical Background and FLAASH-IR

A. Theoretical Background of LST and LSE Retrieval

The interaction with the land surface and the transmission through the atmosphere in the TIR region are not the same as in the reflective region [2]. Nearly all approaches developed to derive LST and LSE from the TIR spectral range are based on the TIR radiative transfer procedure. Therefore, it is important to introduce the TIR radiative transfer model and the retrieval mechanism for LST and LSE retrieval.

1) Forward Radiative Transfer Model: The radiance reaching a sensor onboards an aircraft comes from two sources: the land surface emission and the atmospheric emission. The surface-emitted radiance is a function of its temperature and emissivity, and is disturbed by the absorption and emission of the atmosphere. One disturbance factor is the atmospheric transmittance. The part of atmospheric emission directly reaching

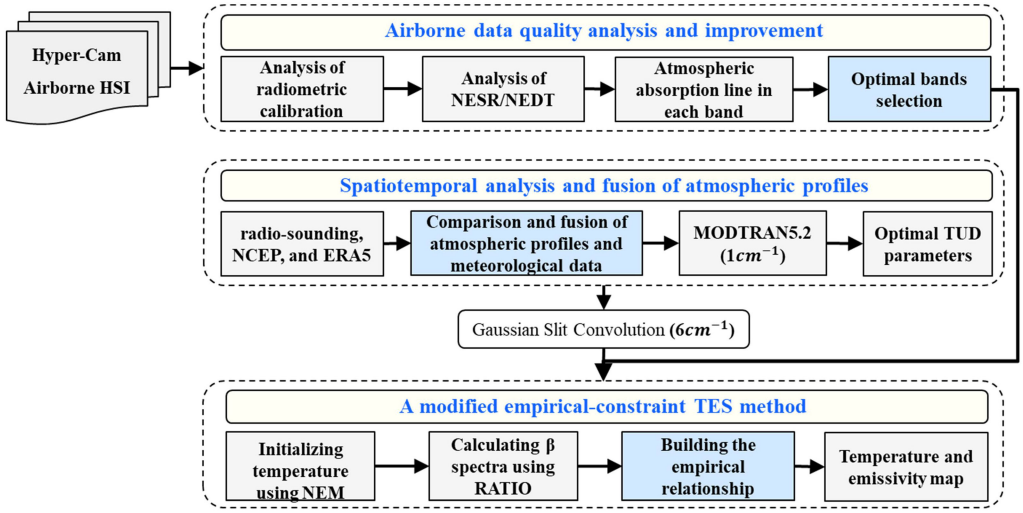

Fig. 5. Processing flowchart of the proposed retrieval framework for Hyper-Cam airborne TIR hyperspectral imagery.

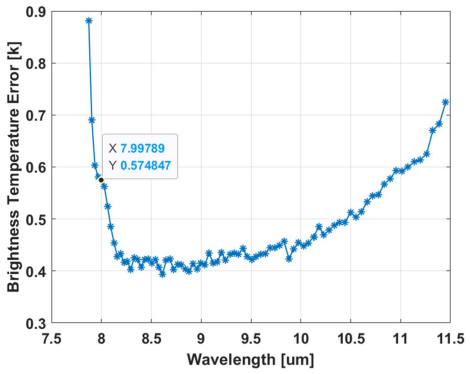

Fig. 6. Estimated radiometric calibration error for each band.

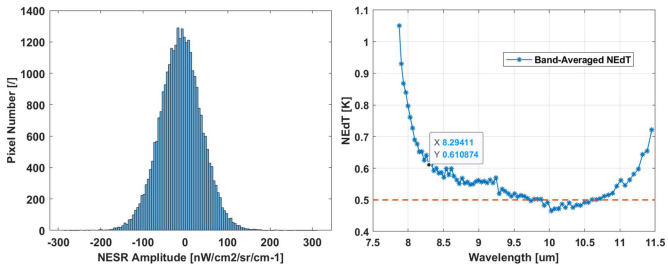

Fig. 7. Estimated measurement noise for the airborne data: (a) histogram of NESR at the 10 μm band and (b) band-averaged NEDT.

the airborne sensor is the upwelling radiance. In addition, the downwelling radiance emitted from the entire atmosphere is reflected back to the sensor by ground objects. The radiance recorded by an airborne sensor can be formulated as the radiative transfer equation (RTE) in the TIR region, as shown in (1):

$$L_s(\lambda) = \varepsilon_G(\lambda) B(\lambda, T_G) \tau(\lambda) + (1 - \varepsilon_G(\lambda)) L_D(\lambda) \tau(\lambda) + L_U(\lambda) \quad (1)$$

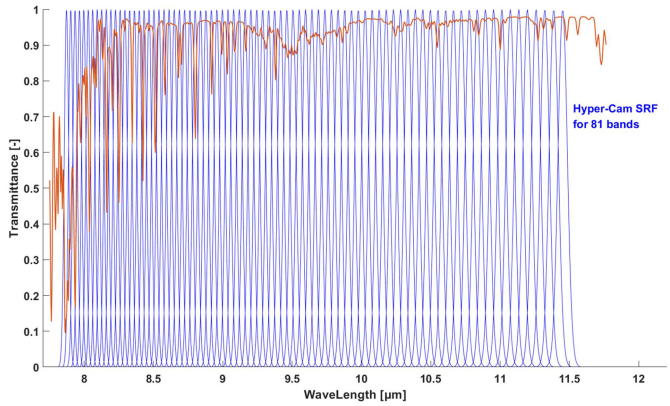

Fig. 8. Location of each band of the experimental imagery compared to the atmospheric effect spectra.

where λ is the wavelength; $\varepsilon_G(\lambda)$ is the emissivity; T_G is the LST; $B(\lambda, T_G)$ is the Planck function; $\tau(\lambda)$ and $L_U(\lambda)$ are, respectively, the total transmittance and the upwelling of the atmosphere between the land surface and the airborne sensor; and $L_D(\lambda)$ is the hemispherical downwelling radiance.

2) Retrieval Mechanism for LST and LSE: The nature of retrieving LST and LSE from airborne TIR hyperspectral imagery is to solve an underdetermined problem. In (1), $L_S(\lambda)$ is the only known quantity, while the five corresponding parameters of $\tau(\lambda,)$ $L_U(\lambda)$, $L_D(\lambda)$, $\varepsilon_G(\lambda)$, and T_G are all unknowns. Therefore, LST and LSE retrieval generally incorporates two steps: 1) AC and 2) TES. The goal of AC is to remove the atmospheric transmittance and upwelling radiance to obtain the ground-leaving radiance $L_G(\lambda)$, as depicted in following equation:

$$L_G(\lambda) = \varepsilon_G(\lambda) B(\lambda, T_G) + (1 - \varepsilon_G(\lambda)) L_D(\lambda) = \frac{L_s(\lambda) - L_U(\lambda)}{\tau(\lambda)}. \quad (2)$$

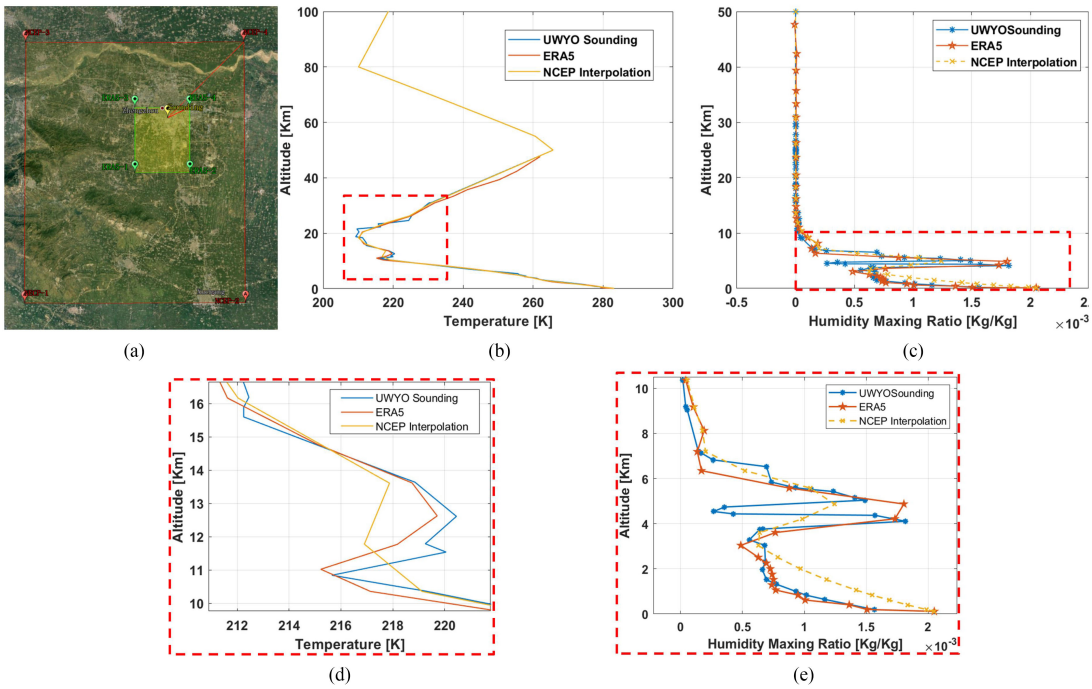

Fig. 9. Comparison between the UWYO radio soundings, the interpolated NCEP data, and the ERA5 atmospheric profiles: (a) atmospheric profile grids of NCEP and ERA5; (b) temperature profiles; (c) humidity profiles; (d) enlarged view of the red box in (b); and (e) enlarged view of the red box in (c).

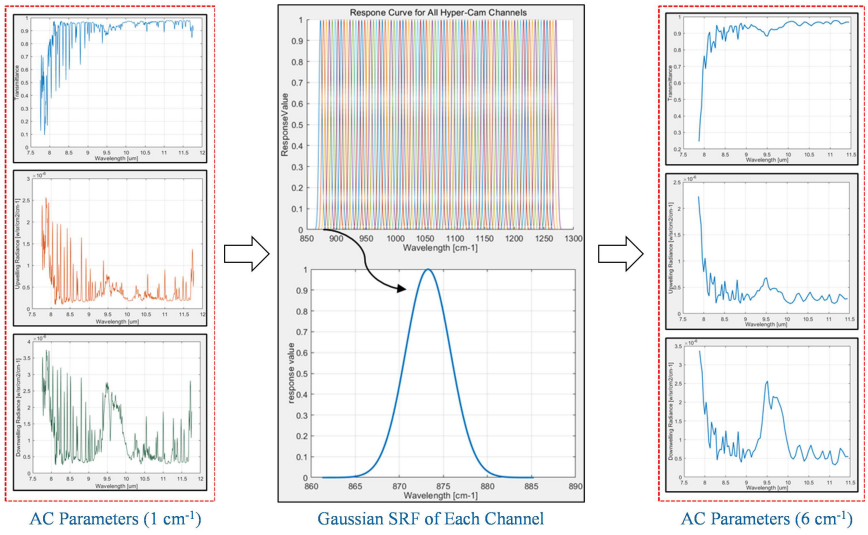

Fig. 10. Simulated AC parameters with high spectral resolution and spectral convolution for the Hyper-Cam date.

The goal of TES is to remove the atmospheric downwelling effect and factor the ground-leaving radiance into the emissivity and temperature. For a given atmospheric model defining the downwelling radiance, the emissivity of each band can be calculated using the following formula:

$$\varepsilon_G(\lambda) = \frac{L_G(\lambda) - L_D(\lambda)}{B(\lambda, T_G) - L_D(\lambda)}. \tag{3}$$

Clearly, LST and LSE retrieval with the ground-leaving radiance is still an underdetermined problem, with $\varepsilon_G(\lambda)$ and T_G unknown, whereas only $L_G(\lambda)$ is known for each band of a pixel. To deal with this problem, some reasonable assumptions or constraints about the "character" of the unknown emissivity spectra should be introduced.

B. FLAASH-IR

FLAASH-IR is an automated retrieval method including both AC and TES. It has been previously applied to the airborne and ground-to-ground TIR hyperspectral imagery taken by the

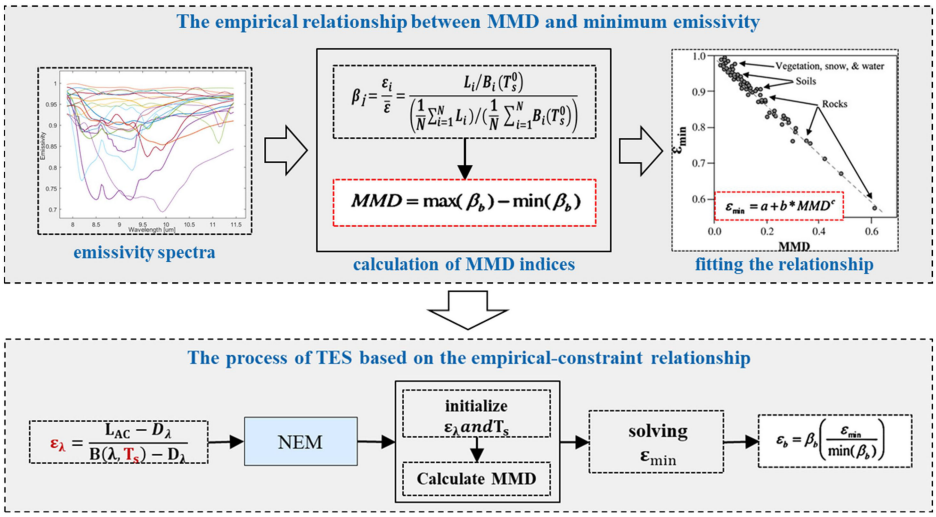

Fig. 11. Flowchart of the empirically constrained TES method.

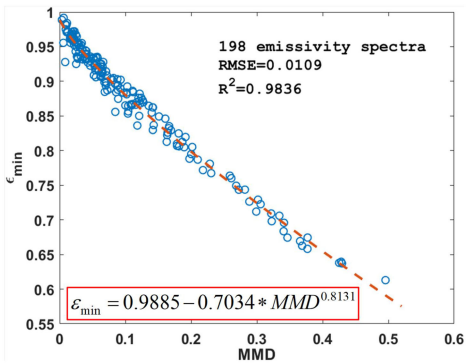

Fig. 12. Fitting relationship between MMD and minimum emissivity.

Hyper-Cam-LW sensor [5], [24]. In the processing procedure of FLAASH-IR, the AC parameters are retrieved from the imagery itself via a look-up table of atmospheric transmittance, upwelling, and downwelling radiance (referred as "TUD LUT"), which is generated by MODTRAN atmospheric simulation. A smoothness criterion based TES algorithm is then used for determining the final LST and LSE. The processing framework of the FLAASH-IR algorithm is shown in Fig. 4.

From Fig. 4, it can be seen that an important feature of this algorithm is that the AC parameters can be estimated from the imagery itself by minimizing the emissivity smoothness for both the surface temperature and the atmospheric variables. The TES method based on a radiance smoothness criterion is then used to determine the LST and LSE values of the entire image. It is therefore clear that both the AC parameter retrieval and the TES are reliant on the smoothness criterion. However, this smoothness criterion is liable to be impacted by noise, leading to the retrieved atmospheric parameters not being in agreement with the real atmospheric conditions. As a result, the final TES results can be unreliable for Hyper-Cam airborne TIR hyperspectral imagery. Therefore, a new processing framework for Hyper-Cam-LW airborne hyperspectral imagery is required.

IV. Proposed Retrieval Framework for Hyper-Cam TIR Hyperspectral Imagery

The proposed processing framework for retrieving LST and LSE from Hyper-Cam LW airborne TIR hyperspectral imagery consists of three parts, as shown in Fig. 5.

The three parts of the proposed framework are: 1) data quality improvement based on band selection; 2) reanalysis profile selection based on spatiotemporal analysis and fusion of three types of widely used profiles; and 3) a modified empirically constrained TES algorithm based on the expansion of the original TES algorithm.

A. Data Quality Analysis and Improvement

The radiometric calibration error, measurement noise, and strong atmospheric absorption in some channels have enormously adverse impacts on LST and LSE retrieval [27], [28]. In this section, these factors are quantitatively analyzed, and we describe how the problematic bands affected by these factors are removed to improve the image quality.

1) Radiometric Calibration Error Analysis: First, the blackbody calibration files acquired during the flight campaign were utilized for the radiometric calibration analysis. The radiometric calibration accuracy was measured by comparing the calibrated radiance spectrum with the theoretical spectrum. As shown in Fig. 6, it is clear that the calibration accuracy is better than 1 K. It should be noted that the calibration error of the bands below 8 μm rapidly becomes larger as the wavelength decreases for the airborne TIR hyperspectral imagery, with an error of between around 0.4 and 1.0 K over the spectral range. This may be due to the instrument internal temperature changes at the start of the measurement.

2) Imagery Measurement Noise Analysis: The noise equivalent spectral radiance and noise equivalent delta temperature (NEDT) were estimated via calculating the standard deviation of the blackbodies. Fig. 7 illustrates the measurement noise for two airborne images. It is clear that the airborne imagery contains

a lot of noise, and the NEDTs are more than 0.5 K over most of the spectral channels. In particular, the noise increases sharply below 8.294 μm, which should be removed for LST and LSE retrieval.

3) Atmospheric Absorption Analysis of Each Band: Finally, the atmospheric absorption intensity was checked for each band, since the atmospheric effect intensity is different for different bands, and some bands located in the strong atmospheric absorption lines cannot be recovered to the original values. Fig. 8 shows the location of each band of the Hyper-Cam airborne imagery, compared to the atmospheric transmittance spectrum. The red curve is the atmospheric transmittance, and the blue curves are the Hyper-Cam spectral response function (SRF) for each band. This demonstrates that the bands of 8.435, 8.5, 8.8, 8.9, 9.37, 9.46, and 9.5 μm are located in the strong atmospheric absorption lines.

To sum up, through the quantitative analysis of the radiometric calibration, measurement noise, and atmospheric absorption lines, it is clear that the bands before 8 μm have a severe calibration problem, and the bands before 8.294 μm contain high measurement noise. In addition, the bands of 8.435, 8.5, 8.8, 8.9, 9.37, 9.46, and 9.5 μm are located in the strong atmospheric absorption lines. Therefore, these bands are all removed and the remaining bands are utilized for the LST and LSE retrieval.

B. Atmospheric Profiles Based on Spatiotemporal Analysis and Fusion

There are no synchronously measured atmospheric profiles available for AC when using the MODTRAN model. In this section, reanalysis atmospheric profiles are analyzed and compared, to replace synchronous sounding profiles. First, according to the flight campaign location and time, an atmospheric profile observation station, i.e., the University of Wyoming (UWYO) ZHCC_57083 sounding station, was selected as the benchmark for the comparison of the different reanalysis atmospheric profiles. Profiles from the National Centers for Environmental Prediction (NCEP) [29] and ERA5 [30] were then, respectively, interpolated to the same position and time as the ZHCC_57083 station, and a comparison of the different profiles was conducted according to the consistency with the sounding profiles. Finally, atmospheric simulation was carried out using the MODTRAN 5.2 model to obtain the AC parameters.

Radio-sounding atmospheric profiles are obtained via physical measurement and can reflect the actual atmospheric conditions of a certain area. The Institute of Atmospheric Sciences at the UWYO provides a global radio-sounding data download platform. There are around 89 UWYO sounding stations all over China, and these stations collect the atmospheric profiles of temperature, pressure, and humidity via sounding balloons at 0:00 UTC and 12:00 UTC every day. Among these stations, the ZHCC_57083 sounding station is located in the downtown area of the city of Zhengzhou, and is the nearest sounding station to the flight area, with a position difference of around 36 km compared with the flight area. In addition, since the atmospheric profiles of temperature, pressure, and humidity at the ZHCC_57083 station are measured at 0:00 UTC, there is a time difference of 3.5 h between the imaging time and the UWYO sounding time.

The NCEP produces global atmospheric profile models on a $1^\circ \times 1^\circ$ grid at 6-h intervals over the course of a day (0:00, 6:00, 12:00, and 18:00 GMT), as shown in the red box in Fig. 9(a). However, the study area does not locate at a grid node, and there is a time difference of 3 h. Compared with the NCEP atmospheric profiles, the ERA5 atmospheric profiles have a higher spatial and temporal resolution, with a horizontal resolution of $0.25^\circ \times 0.25^\circ$ (about 25 km), a vertical resolution of 37 levels, and a temporal resolution of every hour, as shown in the green box in Fig. 9(a). In order to validate the accuracy of the NCEP and ERA5 profiles, the interpolated NCEP and ERA5 profiles were compared with the UWYO sounding profiles, as shown in Fig. 9(b) and (c). It is clear from Fig. 9(b) and (d) that the ERA5 temperature profile is more consistent with the actual sounding temperature profile than the NCEP interpolation profile. As for the humidity profile, differing from satellite remote sensing, the flight height for the TIR hyperspectral imagery is around 2.5 km, and the interferences of atmospheric transmittance and upwelling radiance are mainly related to the water vapor content below a 3-km altitude. It is also clear from Fig. 9(c) and (e) that the humidity mixing ratio of ERA5 is more consistent with the actual sounding humidity profile below a 3-km altitude, and the ERA5 humidity profile has the highest vertical resolution in this altitude range, compared with the sounding and NCEP interpolation profiles. Therefore, the ERA5 profiles should produce the best atmospheric transmittance and upwelling radiance for the AC of the airborne TIR hyperspectral imagery. In addition, since water vapor normally exists below an altitude of 10 km, in this whole altitude range, just one value of ERA5 around the 4.8 km altitude level is quite different from the corresponding value of the sounding humidity profile, and the remaining values are highly consistent with the corresponding sounding values. Therefore, the data from ERA5 have a better coherence with the real sounding profiles than the NCEP data, indicating that the ERA5 product has more accurate atmospheric profiles. In addition, the ERA5 data have higher spatial, temporal, and vertical resolutions. Furthermore, to obtain more accurate atmospheric profiles for AC parameter simulation, the ground-measured meteorological data were fused with the ERA5 data to modify the lower level values.

The selected atmospheric profiles were entered into MODTRAN 5.2 with a spectral resolution of 1 cm^{-1}. However, the spectral resolution of the airborne imagery is 6 cm^{-1}. In practice, a simulated Gaussian SRF is often used for TIR hyperspectral instruments [31], [32]. Therefore, the high spectral resolution AC parameters were convolved with the simulated Gaussian SRF to reconcile the bands of the AC parameters with those of the airborne data, as shown in Fig. 10.

C. Modified Empirically Constrained TES Method

In practice, Hyper-Cam airborne TIR hyperspectral imagery contains a high noise level, with NEDT values of more than 0.5 K

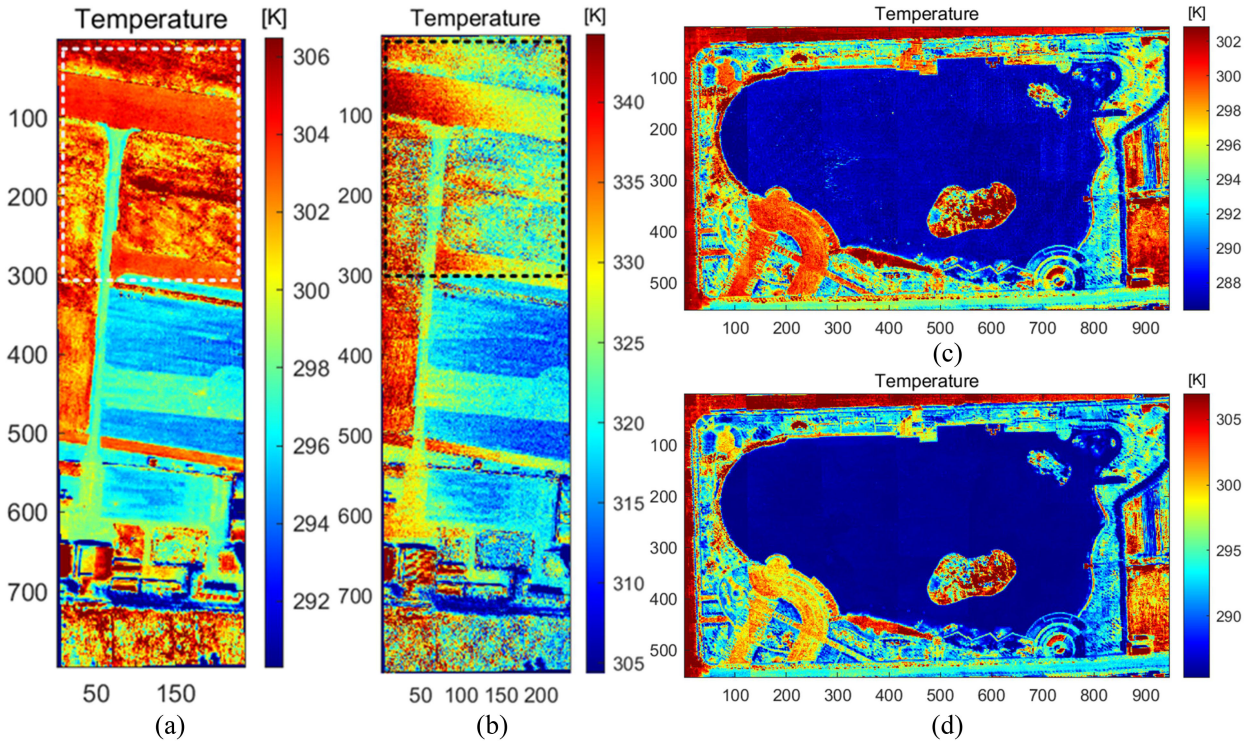

Fig. 13. Temperature maps from the two methods: (a) and (b) are, respectively, the airport site LST maps from the modified method and FLAASH-IR; (c) and (d) are, respectively, the Dongguo Lake site LST maps from the modified method and FLAASH-IR.

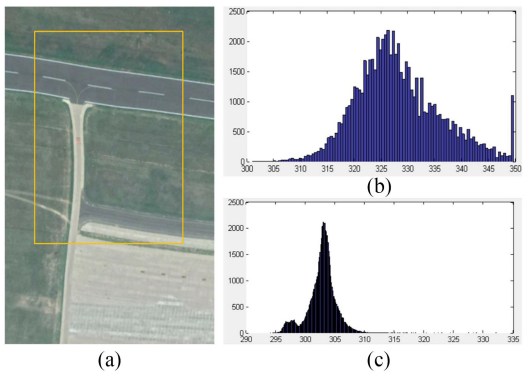

Fig. 14. Temperature distribution histograms for the two methods. (a) Land cover of the AOI. (b) Temperature distribution histogram of FLAASH-IR. (c) Temperature distribution histogram of the modified method.

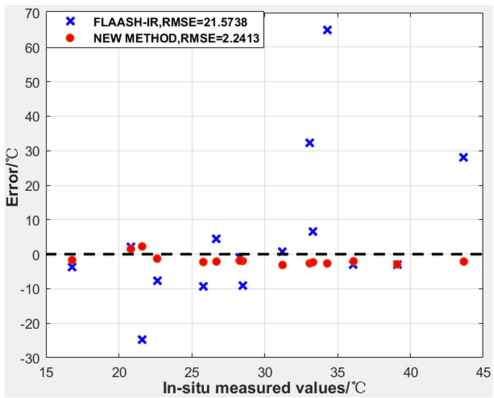

Fig. 15. *In-situ* measurement locations and the retrieval error for FLAASH-IR and the modified method.

for every band, which negatively affects the retrieval results when using the TES methods based on a smoothness criterion. To overcome this disadvantage of the smoothness constraint criterion, a modified empirically constrained TES method is proposed by the expansion of the original TES algorithm for Hyper-Cam airborne TIR hyperspectral imagery. The flowchart of the modified empirically constrained TES method is illustrated in Fig. 11.

The original TES method was initially designed for use with TIR multispectral data, and includes three modules: 1) the normalized emissivity method module; 2) the ratio (RAT) module; and 3) the maximum–minimum relative emissivity difference (MMD) module. Full details of this method are not provided here, and we refer the interested reader to the study by Gillespie *et al*. [20] and other research [33], [34]. The empirical relationship between minimum emissivity value $\varepsilon_{\min}$ and MMD is the key feature of the method, and it needs to be established for specific sensor data. This empirical constraint relationship has been investigated on different sensors with various spectral channels, such as the ASTER sensor [20], the TASI sensor [35], and the HyTES sensor [36]. However, this empirical constraint relationship has not been previously applied to Hyper-Cam

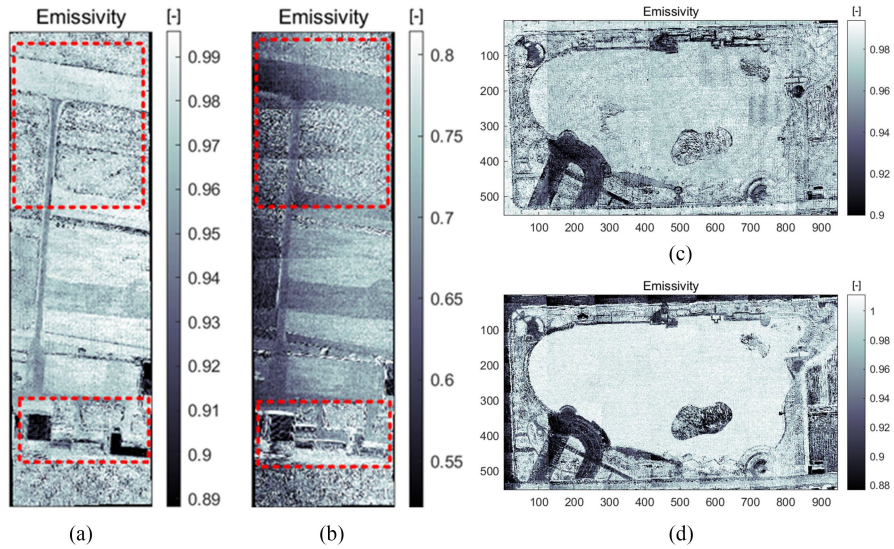

Fig. 16. Emissivity maps from the two methods: (a) and (b) are, respectively, the airport site LSE maps obtained by the modified method and FLAASH-IR; (c) and (d) are, respectively, the Dongguo Lake site LSE maps obtained by the modified method and FLAASH-IR.

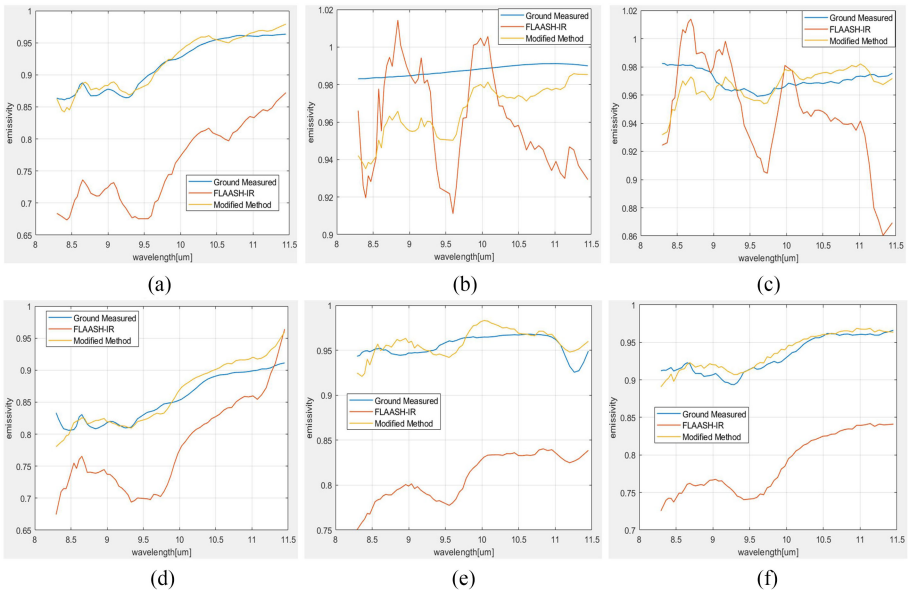

Fig. 17. Comparison between the ground-measured spectra and the retrieved spectra of FLAASH-IR and the modified method: (a) sandy ground, (b) lake water, (c) green vegetation, (d) flagging, (e) asphalt road, and (f) cement road.

airborne hyperspectral data with 81 bands. This relationship was therefore rebuilt to extend the original TES method to Hyper-Cam airborne imagery.

The MMD index represents the absolute value of the difference between the maximum and minimum values of the β spectrum calculated in the RAT module. Normally, noise in Hyper-Cam airborne imagery results in little change for the MMD value. Therefore, the MMD index is less susceptible to noise than the smoothness criterion. There is a stable empirical relationship between the MMD index and the minimum emissivity value $\varepsilon_{\min}$. To obtain reliable parameters for this empirical relationship, 198 spectra extracted from the JHU library were used for fitting the relationship, including water, vegetation, soil, and rock spectra, which were converted to emissivity. As shown in Fig. 12, the empirical relationship for the Hyper-Cam sensor clearly differs from that for the ASTER sensor and TASI sensor, which are both widely used for TIR retrieval. This relationship acts as the empirical constraint in the retrieval of LST and LSE from Hyper-Cam data, instead of the smoothness criterion.

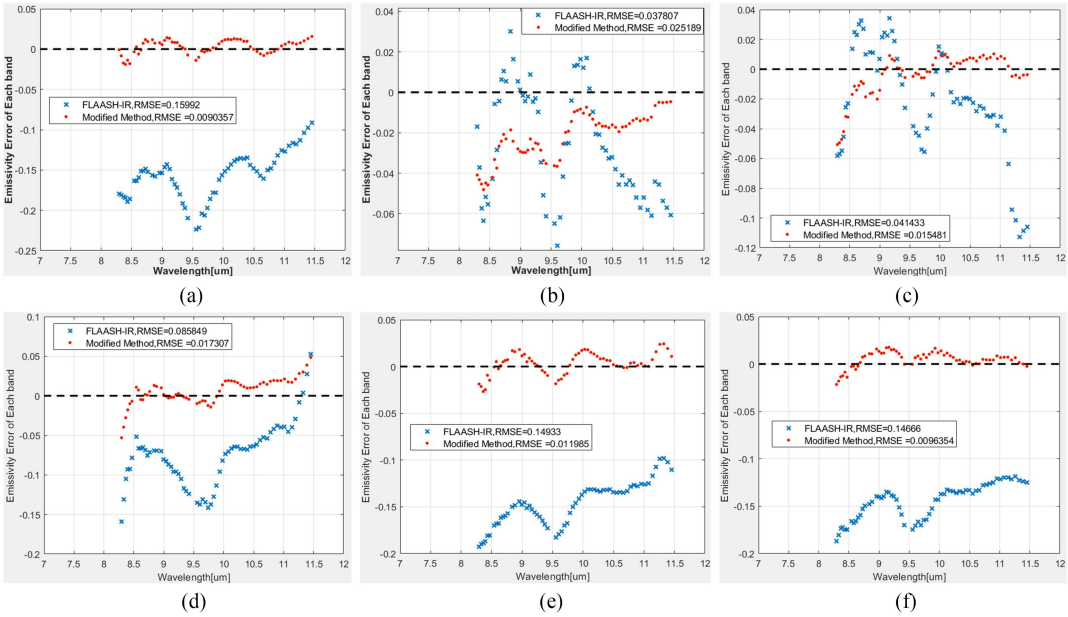

Fig. 18. Band error of the emissivity spectra for FLAASH-IR and the modified method: (a) sandy ground, (b) lake water, (c) green vegetation, (d) flagging, (e) asphalt road, and (f) cement road.

V. Experimental Results and Discussion

To evaluate the performance of the proposed processing framework for Hyper-Cam airborne images, airborne TIR hyperspectral images were collected from two sites in the city of Zhengzhou in 2019, and were then processed by the proposed method and FLAASH-IR. A qualitative and quantitative evaluation was then performed using *in-situ* ground-measured data for the LST and LSE results.

A. Retrieved Temperature Evaluation

The FLAASH-IR temperature results and the *in-situ* measurements were used as the reference for verifying the temperature accuracy of the modified methodology.

1) Qualitative Analysis for the Areas of Interest (AOIs): Areas of interest (AOIs) were selected from the temperature maps to qualitatively compare the capability to distinguish different homogeneous ground covers, as shown in Fig. 13 (marked with boxes). Statistical histograms of the AOIs were also produced to show the temperature distribution of the land surface covered with several uniform materials. A comparison of the LST results obtained by the modified method and the FLAASH-IR method is provided in Fig. 13.

It can be seen that the different surface materials have visible temperature differences for both methods. However, a new asphalt road lies at the top of the airport site, and shows a distinct temperature difference in the FLAASH-IR temperature map [Fig. 13(b)]. The big temperature variation among the same material in one flight line is unreasonable. In contrast, the LST map of the modified method maintains temperature uniformity within the areas of homogeneous ground materials.

As shown in Fig. 14(a), there are four types of homogeneous land covers in the AOI at the airport site: asphalt road, cement road, bare soil, and yellow grass. Normally, these land-cover types would be expected to have a similar temperature. The temperature distribution of the modified method is a bimodal curve with a small temperature range. The large peak is due to the aggregation of the asphalt, cement, and bare soil pixels. In contrast, the statistical result of the FLAASH-IR is a unimodal distribution with a large temperature difference range.

In addition, the average temperature of the FLAASH-IR temperature map is 55.2 °C and the maximum value is 76.65 °C. Taking the land surface atmospheric temperature of 17.6 °C into account, it is apparent that the FLAASH-IR method severely overestimates the LST. Meanwhile, the average temperature of the modified method AOI pixels is 20.92 °C, and the maximum value is 58.9 °C, proving that the modified method can obtain a more reasonable result than the FLAASH-IR method, as shown in Table II.

TABLE II
Statistics of the Temperature Distributions Obtained by the Two Methods for the AOIs

	FLAASH-IR/°C	Modified method/°C
Minimum temperature	28.07	20.92
Maximum temperature	76.65	58.94
Average temperature	55.21	29.65
Median temperature	54.15	29.88
Standard deviation	7.91	2.34
Pixel number	67847	67847

TABLE III
COMPARISON BETWEEN THE RETRIEVED AND MEASURED TEMPERATURES

Sample type	In situ T /℃	FLAASH-IR /℃	Modified method /℃
Lime Road	28.50	19.38	26.56
Old Cement Square	25.80	16.41	23.55
Green Metal Plate	39.10	36	36.17
Blue Metal Plate	36.10	33.20	34.07
Aluminum Plate	21.60	-3.06	23.86
Cement Road	26.70	31.24	24.58
Asphalt Road	33.10	65.26	30.46
Yellow Grass	34.30	99.25	31.63
Bridge	28.30	27.407	26.44
Vegetation	22.63	14.87	21.35
Sand Pond	33.33	39.92	31.00
Lake Water	16.80	13.18	15.1
Rubber Road	43.67	71.74	41.54
Green Grass(lake)	20.83	22.95	22.37
Marble Square	31.23	32.02	28.10
RMSE		21.57	2.24

2) Qualitative Analysis for the AOIs: The results of FLAASH-IR and the modified method were compared to *in-situ* LST measurements for the quantitative evaluation. These land-cover types can be classified into two categories: natural surfaces and artificial surfaces. The reason for choosing these land-cover types for the temperature validation was that they all have a relatively large area to reduce the effect of mixed pixels and avoid the thermal radiance from the surroundings, such as buildings, trees, etc. All the measurements of the land-cover types were made within 5 min of the flight line overpass time. The comparison between the *in-situ* measurements and the corresponding retrieved results is provided in Table III.

In Table III, the temperatures for aluminum plate and rubber road obtained using FLAASH-IR are abnormal temperature values. This may have been caused by the high reflectivity of these materials. The high reflectivity leads to a low signal-to-noise ratio and amplifies the negative effect of the atmospheric downwelling radiance because of the small values of land surface radiance.

The root-mean-square error (RMSE) of the FLAASH-IR results is 21.57 °C, and the LSTs of the highly reflective surfaces are negative. Correspondingly, the RMSE of the modified method is 2.24 °C, which is within a reasonable range, because the measurement time difference and radiometric calibration error may have led to some temperature variation. The maximum difference between the modified method and the ground-measured values is 3.13 °C for the marble square land-cover type. Fig. 15 plots the distribution of the errors for the two TES approaches.

B. Retrieved Emissivity Evaluation

1) Consistency Analysis for Homogeneous Surfaces: The emissivity results of the modified method were first qualitatively compared with the FLAASH-IR results. A quantitative comparison was then conducted with the *in-situ* measured emissivity spectra. The emissivity maps from both methods are shown in Fig. 16, where the red frames illustrate that the LSE maps of the modified method can better distinguish the different land-cover types.

TABLE IV
RMSE OF FLAASH-IR AND THE MODIFIED METHOD

Sample type	RMSE of FLAASH-IR	RMSE of Modified method
Sandy ground	0.15992	0.00904
Lake water	0.03781	0.02519
Green vegetation	0.04143	0.01548
Flagging road	0.08585	0.01731
Asphalt road	0.14933	0.00120
Cement road	0.14666	0.00964

In addition, the LSE shape was assessed by comparing it with the reference spectra, for asphalt, cement, sand, flagging, green grass, and cold lake water. The comparison of the emissivity spectral shapes is provided in Fig. 17. As shown in Fig. 17, the atmospheric residuals are apparent around 9.5 μm and below the range of 8.36 μm for FLAASH-IR, which may have been caused by error in the AC parameter retrieval. In addition, the LSEs are generally underestimated compared with the *in-situ* measurements. In contrast, the results of the modified method show a better performance in restraining the atmospheric residual, indicating that the selection of atmospheric profiles works well for LST and LSE retrieval with Hyper-Cam airborne imagery. The amplitude of the LSE spectra from the modified method shows good agreement with the *in-situ* measurements, indicating that the modified empirically constrained TES method is less susceptible to noise and is able to derive more accurate LST and LSE values.

2) Quantitative Error Analysis: For the quantitative assessment of the LSE, the RMSE of each method was calculated between the ground-measured LSEs and the retrieved LSEs, as shown in Fig. 18 and Table IV. Clearly, FLAASH-IR tends to underestimate the emissivity spectra of the sandy ground, asphalt road, flagging road, and cement road, but it shows a relatively good ability to inverse the ground objects with high emissivity. For example, the retrieved emissivity spectra of the water and green vegetation are in good agreement with the *in-situ* measured spectra. The underestimation of the retrieval emissivity can be attributed to overcompensation of the atmospheric effect and noise effect. The AC parameters are derived from the imagery itself, which are also affected by measurement noise. Because of the underestimation of the emissivity, the RMSE of FLAASH-IR is greater than 0.1, resulting in overestimation of the LST. In contrast, the RMSE of the modified method is mainly below 0.015, which is more accurate. There is, however, the phenomenon that the emissivity error for lake water is high for both FLAASH-IR and the proposed method, which is caused by the high noise contained in the airborne TIR hyperspectral imagery, and the fact that the emissivity spectrum of water has low spectral contrast.

VI. Conclusion

Airborne TIR hyperspectral sensors have distinct advantages over spaceborne sensors in acquiring high spatial and spectral resolution imagery, which contributes to extracting more accurate LST and LSE via taking advantage of the contiguous spectral bands. In this article, a type of FTIR imager was used for acquiring a set of airborne TIR hyperspectral images in the 7.5–11.5 μm range in China, on March 30, 2019. In addition, a practical LST and LSE retrieval framework incorporating reanalysis atmospheric profiles has been proposed for Hyper-Cam airborne TIR hyperspectral imagery. First, the airborne TIR hyperspectral imagery quality is improved through data quality analysis and band selection. Then, to overcome the lack of synchronously measured atmospheric sounding profiles, three types of reanalysis atmospheric profiles are compared, and the optimal atmospheric profiles and ground meteorological data are fused to replace the synchronously measured sounding profiles. Finally, an empirically constrained TES method is proposed to expand the application of the original TES algorithm, which was initially designed for multispectral data.

The comparison conducted in this article indicated that the emissivity RMSE of the modified method was mainly below 0.015, and the temperature RMSE of all the ground samples was about 2.2 K, proving that the proposed method can greatly improve the retrieval accuracy for Hyper-Cam airborne data, compared with FLAASH-IR. In addition, the modified method has the advantages of being able to effectively suppress the atmospheric influence, and it is less susceptible to measurement noise. From these results, some conclusions can be drawn: 1) a band selection operation is needed to improve the Hyper-Cam airborne TIR hyperspectral data, since the measurement noise, radiometric calibration error, and strong atmospheric absorption can reduce the image quality in certain bands; 2) the spatiotemporal analysis and selection of ERA5 and NCEP atmospheric profiles is a better choice for AC when there are no synchronous radio-sounding profiles available; and 3) the empirically constrained relationship between MMD and minimum emissivity is suitable for airborne data with a relatively high noise level.

In the future, improvement of the radiometric calibration will be attempted for this set of airborne TIR hyperspectral imagery. Furthermore, comprehensive denoising of airborne TIR hyperspectral imagery will be studied to further improve the current image quality.

Acknowledgment

The authors would like to thank Shugui Zhou of Zhengzhou University for his help in the process of data processing.

References

[1] H. Ren *et al.*, "Retrieval of land surface temperature, emissivity, and atmospheric parameters from hyperspectral thermal infrared image using a feature-band linear-format hybrid algorithm," *IEEE Trans. Geosci. Remote Sens.*, vol. 60, pp. 1–15, Jan. 2021.

[2] D. Manolakis *et al.*, "Longwave infrared hyperspectral imaging: Principles, progress, and challenges," *IEEE Geosci. Remote Sens. Mag.*, vol. 7, no. 2, pp. 72–100, Jun. 2019.

[3] J. Cui *et al.*, "Temperature and emissivity separation and mineral mapping based on airborne TASI hyperspectral thermal infrared data," *Int. J. Appl. Earth Observ. Geoinf.*, vol. 40, pp. 19–28, 2015.

[4] M. L. Clark, J. Buck-Diaz, and J. Evens, "Mapping of forest alliances with simulated multi-seasonal hyperspectral satellite imagery," *Remote Sens. Environ.*, vol. 210, pp. 490–507, 2018.

[5] S. Adler-Golden, P. Conforti, M. Gagnon, P. Tremblay, and M. Chamberland, "Remote sensing of surface emissivity with the telops Hyper-Cam," in *Proc. 6th Workshop Hyperspectral Image Signal Process., Evol. Remote Sens.*, 2014, pp. 1–4.

[6] A. Cicone, J. Liu, and H. Zhou, "Hyperspectral chemical plume detection algorithms based on multidimensional iterative filtering decomposition," *Philos. Trans. Roy. Soc. A, Math., Phys. Eng. Sci.*, vol. 374, no. 2065, 2016, Art. no. 20150196.

[7] M. Diani, M. Moscadelli, and G. Corsini, "Improved alpha residuals for target detection in thermal hyperspectral imaging," *IEEE Geosci. Remote Sens. Lett.*, vol. 15, no. 5, pp. 779–783, May 2018.

[8] Z.-L. Li *et al.*, "Satellite-derived land surface temperature: Current status and perspectives," *Remote Sens. Environ.*, vol. 131, pp. 14–37, 2013.

[9] Y. Li, T. Liu, M. E. Shokr, Z. Wang, and L. Zhang, "An improved single-channel polar region ice surface temperature retrieval algorithmusing landsat-8 data," *IEEE Trans. Geosci. Remote Sens.*, vol. 57, no. 11, pp. 8557–8569, Nov. 2019.

[10] R. A. D. Sofla and M. Akhoondzadeh, "Developed split window method to retrieve land surface temperature from HYTES thermal hyperspectral images using genetic algorithm," *Int. J. Remote Sens.*, vol. 40, no. 16, pp. 6249–6261, 2019.

[11] D. Rosario, J. Romano, and C. Borel, "First observations using SPICE hyperspectral dataset," in *Algorithms and Technologies for Multispectral, Hyperspectral, and Ultraspectral Imagery XX*, vol. 9088. Bellingham, WA, USA: International Society for Optics and Photonics, 2014, p. 90880.

[12] C. Liu *et al.*, "New airborne thermal-infrared hyperspectral imager system: Initial validation," *IEEE J. Sel. Topics Appl. Earth Observ. Remote Sens.*, vol. 13, pp. 4149–4165, Jul. 2020.

[13] A. French, J. Norman, and M. Anderson, "A simple and fast atmospheric correction for spaceborne remote sensing of surface temperature," *Remote Sens. Environ.*, vol. 87, no. 2/3, pp. 326–333, 2003.

[14] N. K. Malakar and G. C. Hulley, "A water vapor scaling model for improved land surface temperature and emissivity separation of MODIS thermal infrared data," *Remote Sens. Environ.*, vol. 182, pp. 252–264, 2016.

[15] S. J. Young, B. R. Johnson, and J. A. Hackwell, "An in-scene method for atmospheric compensation of thermal hyperspectral data," *J. Geophys. Res., Atmos.*, vol. 107, no. D24, pp. ACH 14-1–ACH 14-20, 2002.

[16] J. Yang *et al.*, "Evaluation of seven atmospheric profiles from reanalysis and satellite-derived products: Implication for single-channel land surface temperature retrieval," *Remote Sens.*, vol. 12, no. 5, 2020, Art. no. 791.

[17] A. Berk, P. Conforti, R. Kennett, T. Perkins, F. Hawes, and J. van den Bosch, "MODTRAN 6: A major upgrade of the MODTRAN radiative transfer code," in *Proc. 6th IEEE Workshop Hyperspectral Image Signal Process.: Evol. Remote Sens.*, 2014, pp. 1–4.

[18] S. Chen, H. Ren, X. Ye, J. Dong, and Y. Zheng, "Geometry and adjacency effects in urban land surface temperature retrieval from high-spatial-resolution thermal infrared images," *Remote Sens. Environ.*, vol. 262, 2021, Art. no. 112518.

[19] C. C. Borel, "Iterative retrieval of surface emissivity and temperature for a hyperspectral sensor," Office of Scientific & Technical Information Tech. Rep., LA-UR–97-3012, U.S. Dept. Energy, Washington, DC, USA, 1997.

[20] A. Gillespie, S. Rokugawa, T. Matsunaga, J. S. Cothern, S. Hook, and A. B. Kahle, "A temperature and emissivity separation algorithm for advanced spaceborne thermal emission and reflection radiometer (ASTER) images," *IEEE Trans. Geosci. Remote Sens.*, vol. 36, no. 4, pp. 1113–1126, Jul. 1998.

[21] E. D. S. Hernandez-Baquero and R. John, "Atmospheric compensation for surface temperature and emissivity separation," in *Algorithms for Multispectral, Hyperspectral, and Ultraspectral Imagery VI*, vol. 4049. Bellingham, CA, USA: International Society for Optics and Photonics, 2000, pp. 400–410.

[22] N. Wang, H. Wu, F. Nerry, C. Li, and Z.-L. Li, "Temperature and emissivity retrievals from hyperspectral thermal infrared data using linear spectral emissivity constraint," *IEEE Trans. Geosci. Remote Sens.*, vol. 49, no. 4, pp. 1291–1303, Apr. 2011.

[23] E. Puckrin *et al.*, "Airborne measurements in the infrared using FTIR-based imaging hyperspectral sensors," in *Electro-Optical Remote Sensing, Photonic Technologies, and Applications III*, vol. 7482. Bellingham, CA, USA: International Society for Optics and Photonics, 2009, p. 74820S.
[24] S. M. Adler-Golden, P. Conforti, M. Gagnon, P. Tremblay, and M. Chamberland, "Long-wave infrared surface reflectance spectra retrieved from telops hyper-cam imagery," in *SPIE Defense + Security*, vol. 9088. Bellingham, CA, USA: SPIE, 2014, p. 8.
[25] C. C. Borel, "ARTEMISS—An algorithm to retrieve temperature and emissivity from hyper-spectral thermal image data," in *Proc. 28th Annu. GOMACTech. Conf. Hyperspectral Imag. Session*, 2003, pp. 1–4.
[26] A. M. Baldridge, S. Hook, C. Grove, and G. Rivera, "The ASTER spectral library version 2.0," *Remote Sens. Environ.*, vol. 113, no. 4, pp. 711–715, 2009.
[27] P. M. Ingram and A. H. Muse, "Sensitivity of iterative spectrally smooth temperature/emissivity separation to algorithmic assumptions and measurement noise," *IEEE Trans. Geosci. Remote Sens.*, vol. 39, no. 10, pp. 2158–2167, Oct. 2001.
[28] X. OuYang, N. Wang, H. Wu, and Z.-L. Li, "Errors analysis on temperature and emissivity determination from hyperspectral thermal infrared data," *Opt. Exp.*, vol. 18, no. 2, pp. 544–550, 2010.
[29] H. Li, Q. Liu, Y. Du, J. Jiang, and H. Wang, "Evaluation of the NCEP and MODIS atmospheric products for single channel land surface temperature retrieval with ground measurements: A case study of HJ-1B IRS data," *IEEE J. Sel. Topics Appl. Earth Observ. Remote Sens.*, vol. 6, no. 3, pp. 1399–1408, Jun. 2013.
[30] H. Hersbach *et al.*, "The ERA5 global reanalysis," *Quart. J. Roy. Meteorol. Soc.*, vol. 146, no. 730, pp. 1999–2049, 2020.
[31] J. A. Sobrino, J. C. Jiménez-Muñoz, P. J. Zarco-Tejada, G. Sepulcre-Cantó, and E. de Miguel, "Land surface temperature derived from airborne hyperspectral scanner thermal infrared data," *Remote Sens. Environ.*, vol. 102, no. 1, pp. 99–115, 2006.
[32] H. Wang, Q. Xiao, H. Li, and B. Zhong, "Temperature and emissivity separation algorithm for TASI airborne thermal hyperspectral data," in *Proc. Int. Conf. Electron. Commun. Control*, 2011, pp. 1075–1078.
[33] S. P. Grigsby, G. C. Hulley, D. A. Roberts, C. Scheele, S. L. Ustin, and M. M. Alsina, "Improved surface temperature estimates with MASTER/AVIRIS sensor fusion," *Remote Sens. Environ.*, vol. 167, pp. 53–63, 2015.
[34] W. T. Gustafson, A. R. Gillespie, and G. J. Yamada, "Revisions to the ASTER temperature/emissivity separation algorithm," in *Proc. 2nd Int. Symp. Recent Adv. Quantitative Remote Sens.*, 2006, Art. no. 1.
[35] H. Yang *et al.*, "Temperature and emissivity separation from thermal airborne hyperspectral imager (TASI) data," *Photogramm. Eng. Remote Sens.*, vol. 79, pp. 1099–1107, 2013.
[36] S. Meerdink *et al.*, "Plant species' spectral emissivity and temperature using the hyperspectral thermal emission spectrometer (HyTES) sensor," *Remote Sens. Environ.*, vol. 224, pp. 421–435, 2019.

Lyuzhou Gao (Member, IEEE) received the B.S. and M.S. degrees in educational technology from Wuhan Sports University and Central China Normal University, Wuhan, China, in 2015 and 2018, respectively. He is currently working toward the Ph.D. degree in photogrammetry and remote sensing at the State Key Laboratory of Information Engineering in Surveying, Mapping and Remote Sensing, Wuhan University, Wuhan, China.

His research interests include airborne thermal infrared hyperspectral imaging, temperature and emissivity retrieval, atmospheric correction, and target detection and identification.

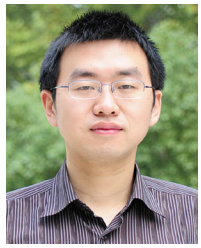

Yanfei Zhong (Senior Member, IEEE) received the B.S. degree in information engineering and the Ph.D. degree in photogrammetry and remote sensing from Wuhan University, Wuhan, China, in 2002 and 2007, respectively.

Since 2010, he has been a Full Professor with the State Key Laboratory of Information Engineering in Surveying, Mapping and Remote Sensing, Wuhan University, Wuhan, China. He organized the Intelligent Data Extraction, Analysis and Applications of Remote Sensing Research Group. He has authored/coauthored more than 100 research papers in international journals. His research interests include hyperspectral remote sensing information processing, high-resolution remote sensing image understanding, and geoscience interpretation for multisource remote sensing data and applications.

Liqin Cao received the M.Sc. and Ph.D. degrees in photogrammetry and remote sensing from Wuhan University, Wuhan, China, in 2006 and 2009, respectively.

From 2015 to 2016, he worked as a Visiting Research Fellow with the Department of Information and Communication Technology, University of Agder (UiA), Grimstad, Norway. She is currently working with the School of Printing and Packaging, Wuhan University. Her research interests include thermal infrared remote sensing, data processing, and image processing.

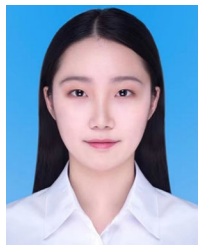

Jiani He received the B.S. degree in geographic information science from the Nanjing University of Posts and Telecommunications, Nanjing, China, in 2019, and the M.S. degree in surveying and mapping engineering from the State Key Laboratory of Information Engineering in Surveying, Mapping and Remote Sensing, Wuhan University, Wuhan, China, in 2021.

She is currently an Engineering Specialist with the Research Center for Intelligent Sensing System with Intelligent Perception Research Institute, Zhejiang Lab, Hangzhou, China. Her research interests include thermal infrared hyperspectral image classification and image registration and mosaic.

Xuhe Zhu received the B.E. and M.Eng. degrees in photogrammetry and remote sensing from Wuhan University, Wuhan, China, in 2018 and 2021, respectively.

He is currently working with Guangzhou Urban Planning and Design Survey Research Institute. His research interests include thermal infrared hyperspectral target detection, image registration and mosaic, and construction of three-dimensional model of tilt photogrammetry.